Earth, Planets and Space

EXPRESS LETTER

Inelastic deformation zone in the lower crust for the San-in Shear Zone, Southwest Japan, as observed by a dense GNSS network

Angela Meneses-Gutierrez[1,2*] and Takuya Nishimura[3]

Abstract

We analyze Global Navigation Satellite System (GNSS) within the San-in Shear Zone (SSZ), Southwest Japan, in order to clarify the width of the inelastic deformation zone in the lower crust beneath it. We assumed multiple discrete fault dislocations distributed below the seismogenic depth in a channel to represent inelastic deformation in the lower crust. Kinematic models at 68% confidence level at three profiles indicate that deformation can be explained by a deep inelastic deformation zone with a width of 0.5–56.0 km, 0.5–79.5 km, and 0.0–58.5 km, for the Eastern, Central and Western profiles, respectively; and a relative moving rate between the two blocks sandwiching the zone of 6.2–8.0 mm/year. In Eastern Tottori, the center of the estimated inelastic zone coincides with the source region of the 1943 Tottori earthquake. In Central and Western Tottori, the channel is in agreement with the source regions of the 2000 Western and the 2016 Central Tottori earthquake. Current GNSS network provides a limited contribution to constraining the width of the deformation in the lower crust.

Keywords: San-in Shear Zone, GNSS, Intraplate deformation, Strain concentration

Introduction

The existence of a strain concentration zone along the San-in district in Southwest Japan, the San-in Shear Zone (SSZ) (Fig. 1), has been identified from the nationwide Global Navigation Satellite System (GNSS) Earth Observation Network System (GEONET) data (Nishimura and Takada 2017). This concentration zone is a ~50 km width right-lateral shear zone, where high seismicity has been reported (e.g., Kawanishi et al. 2009), hosting 17 crustal earthquakes with magnitude larger than 6 for the last 100 years. Despite the general right-lateral motion observed in the SSZ, recent seismic events in the area occurred on NNW–SSE trending sinistral faults. This behavior has been interpreted as conjugated Riedel Shears in the shear zone and it indicates that the SSZ is young on geological time scales (Nishimura and Takada 2017).

No major active fault has been identified in the SSZ. However, quantitative models of the observed horizontal displacements at GEONET stations in the deformation zone indicates that a ~5 mm/year deep creep on a vertical fault with right-lateral motion can explain deformation in the area (Nishimura and Takada 2017). The model proposed by Nishimura and Takada (2017) consists of creep on a vertical fault plane with no thickness from a locking depth to infinite depth, which is originally proposed by Savage and Burford (1973) and often used to reproduce surface deformation around a vertical strike–slip fault. However, it is expected that a shear deformation below a seismogenic depth occurs within a distinctive width according to geological observation of a mylonite and ultramylonite zone of an exhumed fault (cf. Bürgmann and Dresen 2008) and numerical simulation using rheology of the lower crust (Zhang and Sagiya 2017). In the SSZ Kawanishi et al. (2009) suggested aseismic movement in a ductile shear zone with a width of ≤ 20 km below the seismogenic depth. Their model explains a systematic shift in the azimuth of the

*Correspondence: angela@seis.nagoya-u.ac.jp
[1] Institute for Advanced Research, Nagoya University, Nagoya, Japan
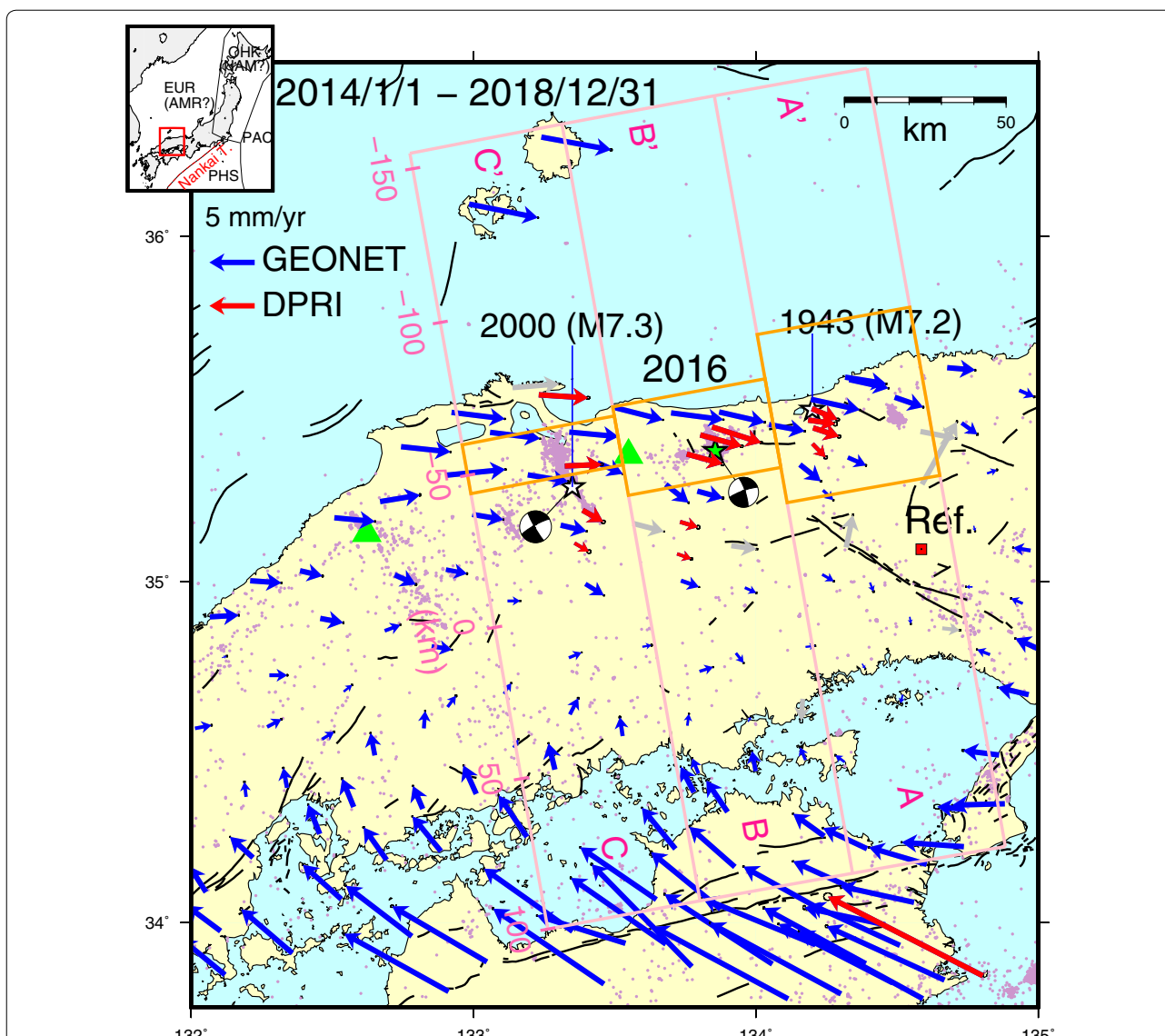Full list of author information is available at the end of the article

Fig. 1 GNSS velocities in and around the San-in Shear Zone from January 2014 to December 2018 with respect to station 0344 (red diamond). Blue arrows denote GEONET data, while red arrows Kyoto University data. Gray arrows represent outliers. Thin black lines denote active Quaternary fault traces (Research Group for Active Faults of Japan 1991). Violet dots denote crustal seismicity (depth < 30 km) from 1998 to 2018. Green triangles are active volcanoes within the SSZ. Stars represent the epicenters of the 1943 Tottori, the 2000 Western Tottori and the 2016 Central Tottori earthquakes. Focal mechanisms for the 2000 and the 2016 events are also shown within the figure. The inset figure shows the location of the study area with respect to the Japanese Islands. Three pink rectangles from A–A′ to C–C′ indicate locations of velocity profiles in Fig. 2. Ticks on lines in the rectangles are plotted with an interval of 50 km. Orange rectangles denote the optimum widths of the ductile zone in the lower crust

maximum principal stress estimated using a focal mechanism of small earthquakes in the aftershock region of the 2000 M_w 6.6 Western Tottori earthquake.

GEONET has allowed the identification and continuous monitoring of multiple crustal deformation processes (e.g., Sagiya et al. 2000). However, the network has its limitations when it comes to resolving small-scale deformation patterns, due to the average spacing between the

GEONET stations being 20 km. Recognizing this limitation, our research group constructed 13 continuous GNSS sites in the SSZ in 2014 for the purpose of providing a better characterization of the crustal deformation pattern in the area (Fig. 1).

In this study, we aim to characterize the width of the deformation in the lower crust beneath the SSZ using GNSS data available in the area. We show that inelastic

deformation in the lower crust is distributed in a channel beneath the SSZ, with a relative motion between the two blocks constraining the inelastic zone of 6.2–8.0 mm/year.

In the following, we introduce the data used for the analysis. We then present the methodology to evaluate the width of the inelastic deformation. Finally, we provide an interpretation of the results.

Data analysis and methodology

We analyze daily coordinates of 100 continuous GNSS stations around the SSZ from 1 January 2014 to 31 December 2018. The network consists of 87 GEONET stations and 13 original stations in the SSZ operated by Disaster Prevention Research Institute, Kyoto University since 2014 near the source regions of the 2000 Western Tottori (M_w 6.6) and the 2016 Central Tottori (M_w 6.2) earthquakes (Fig. 1). Precise daily coordinates for the GNSS sites are calculated with the GNSS-Inferred Positioning System and Orbit Analysis Simulation Software (GIPSY-OASIS), version 6.4 using the Precise Point Positioning processing strategy with ambiguity resolution (Zumberge et al. 1997; Bertiger et al. 2010). Precise satellite orbits, Earth orientation parameters, and satellite clock corrections were obtained from the final solutions provided by the Jet Propulsion Laboratory.

During the analyzed time period, two significant earthquakes affected the crustal deformation in the target area: the M_w 7.1 Kumamoto earthquake sequence in April 2016 (mainshock: 32.76° N, 130.76° E, depth = 11 km, National Research Institute for Earth Science and Disaster Resilience, 2016a) and the M_w 6.2 Central Tottori earthquake on 21 October 2016 (35.38° N, 133.86° E, depth = 11 km, National Research Institute for Earth Science and Disaster Resilience 2016b). Thus, in order to estimate horizontal velocities, we consider the following function for the fitting of each daily coordinate component (i) at each station (n):

$$
\begin{aligned}
u_n^i(t) = a_n^i + b_n^i t &+ c_n^i \sin\left(\frac{2\pi t}{365.25}\right) + d_n^i \cos\left(\frac{2\pi t}{365.25}\right) \\
&+ \sum_{K=1}^{m} e_{n,k}^i H\left(t - t_n^k\right) + \sum_{j=1}^{me} f_{n,j}^i H\left(t - t_{eq}^j\right) \\
&+ g_{n,j}^i H\left(t - t_{eq}^j\right) \ln\left(1 + +\frac{t - t_{eq}^j}{t_{DC}^j}\right)
\end{aligned}
\tag{1}
$$

Here t is given in days. The first two terms on the right correspond to the linear trend, the next three are the seasonal annual variation and the steps related to instrumental changes, and the last two terms are the coseismic

and postseismic displacements for any given earthquakes. In our case, we consider that the postseismic displacement evolves logarithmically with time as expected from afterslip (Marone et al. 1991). t_{eq}^j denotes the origin time of the jth earthquake and t_{DC}^j is the time decay constant for the postseismic process. As we are only interested in the linear fit, we first estimate t_{DC}^j separately and solve Eq. (1) using the value.

For the Kumamoto earthquake, we determine the time decay constant using 150 days of data after the earthquake. We assume that the spatial pattern of the afterslip process does not change with time and estimate the time decay constant using stations 0075, 0399 and 0658, which are located to the westmost of our research area, closer to the source region of the Kumamoto earthquake. We found the time decay constant to be 63.2 days. For the earthquake in Central Tottori, Meneses-Gutierrez et al. (2019) analyzed 7 months of daily coordinates after the 2016 Central Tottori earthquake under the assumption that the postseismic deformation was caused by the afterslip only and estimated the time decay constant to be 2.2 days. We adopt this value for our calculation. The Akaike Information Criterion is used to determine whether coseismic and/or postseismic corrections are necessary at each station for each seismic event (Akaike 1974).

Horizontal displacement rates are calculated for all stations using linear regression with respect to site 0344 (35.09° N, 134.59° E, Fig. 1, Additional file 1: Figure S1, Table 1). Profiles across the region show a trend across the region, with higher gradient to the north (Additional file 1: Figure S1). This pattern reflects the viscous relaxation effect associated with the 2011 M_w 9.0 Tohoku-oki earthquake (38.10° N, 142.86° E, depth = 24 km, National Research Institute for Earth Science and Disaster Resilience 2011). Suito (2017) studied the postseismic deformation related with the Tohoku-oki earthquake observed at GNSS stations employing three-dimensional viscoelastic models with different characteristics. In his analysis, he found that a depth-dependent viscosity model can explain far-field and near-field data as well (Model 4 in Suito 2017). We employ this model to correct for the postseismic deformation of the 2011 Tohoku-oki earthquake in our data (Table 1).

Figure 1 shows the horizontal velocities with respect to the 0344 station after the effect from the 2011 Tohoku-oki event has been removed. Large deformation can be observed in the southern part of Fig. 1, due to the subduction of the Philippine Sea plate (e.g., Yoshioka and Matsuoka 2013). To the north, near East–West motion is observed. Deformation in this area corresponds to the previously identified SSZ (Nishimura and

Table 1 Coordinates and observed horizontal displacement rates of GNSS stations used for modeling before and after removing the effect of the 2011 Tohoku-oki earthquake

Station name	Longitude (°)	Latitude (°)	Uncorrected velocities		Corrected velocities	
			E–W (mm/year)	N–S (mm/year)	E–W (mm/year)	N–S (mm/year)
0074	133.059	35.434	5.53 ± 0.06	− 0.90 ± 0.06	5.52 ± 0.06	− 0.68 ± 0.06
0346	134.403	34.998	0.08 ± 0.10	− 1.05 ± 0.10	0.39 ± 0.10	− 1.01 ± 0.10
0350	134.545	34.897	− 0.39 ± 0.06	− 0.82 ± 0.08	0.11 ± 0.06	− 0.77 ± 0.08
0357	134.520	34.670	− 1.23 ± 0.07	− 1.07 ± 0.07	− 0.22 ± 0.07	− 0.94 ± 0.07
0378	134.047	35.457	4.52 ± 0.09	− 0.79 ± 0.08	3.93 ± 0.09	− 0.74 ± 0.08
0379	133.439	35.346	2.78 ± 0.06	− 1.37 ± 0.07	2.78 ± 0.06	− 1.22 ± 0.07
0380	134.237	35.266	1.38 ± 0.07	− 1.11 ± 0.08	1.15 ± 0.07	− 1.09 ± 0.08
0381	133.309	35.165	2.51 ± 0.06	− 0.82 ± 0.08	2.86 ± 0.06	− 0.67 ± 0.08
0382	133.240	36.285	9.42 ± 0.14	− 1.87 ± 0.12	7.69 ± 0.14	− 1.40 ± 0.12
0383	132.984	36.093	8.73 ± 0.07	− 1.93 ± 0.07	7.58 ± 0.07	− 1.51 ± 0.07
0389	133.792	35.264	2.86 ± 0.12	− 0.87 ± 0.13	2.82 ± 0.12	− 0.78 ± 0.13
0391	134.235	35.021	0.99 ± 0.07	− 0.79 ± 0.08	1.28 ± 0.07	− 0.74 ± 0.08
0392	133.735	35.003	1.48 ± 0.06	− 0.81 ± 0.06	2.00 ± 0.06	− 0.70 ± 0.06
0393	133.960	34.983	0.74 ± 0.09	− 0.66 ± 0.10	1.26 ± 0.08	− 0.58 ± 0.09
0394	133.598	34.810	0.09 ± 0.09	0.05 ± 0.11	1.01 ± 0.09	0.18 ± 0.11
0395	133.929	34.791	0.01 ± 0.06	− 1.20 ± 0.06	0.86 ± 0.06	− 1.09 ± 0.06
0398	133.120	34.943	0.60 ± 0.08	− 0.16 ± 0.07	1.40 ± 0.08	0.01 ± 0.07
0655	134.325	35.361	2.54 ± 0.07	− 0.88 ± 0.11	2.01 ± 0.07	− 0.88 ± 0.11
0662	133.396	34.993	1.43 ± 0.08	− 1.40 ± 0.07	2.05 ± 0.08	− 1.26 ± 0.07
0664	133.338	34.778	0.39 ± 0.06	0.43 ± 0.06	1.41 ± 0.06	0.59 ± 0.06
0765	134.176	34.810	0.28 ± 0.06	0.02 ± 0.08	1.08 ± 0.06	0.12 ± 0.08
0766	133.757	34.579	− 1.12 ± 0.07	1.14 ± 0.06	0.17 ± 0.07	1.30 ± 0.06
1006	134.376	34.760	− 0.48 ± 0.06	− 0.67 ± 0.08	0.34 ± 0.06	− 0.57 ± 0.08
1014	134.195	35.529	6.24 ± 0.07	− 1.20 ± 0.07	5.38 ± 0.07	− 1.17 ± 0.07
1015	133.495	35.507	5.82 ± 0.06	− 1.54 ± 0.07	5.46 ± 0.06	− 1.39 ± 0.07
1016	133.870	35.493	5.59 ± 0.09	− 1.23 ± 0.09	5.03 ± 0.09	− 1.14 ± 0.09
1017	134.156	35.341	2.66 ± 0.09	− 1.87 ± 0.10	2.30 ± 0.09	− 1.84 ± 0.10
1019	133.192	35.311	4.28 ± 0.07	− 0.90 ± 0.07	4.44 ± 0.07	− 0.73 ± 0.07
1026	133.681	35.283	2.49 ± 0.07	− 2.12 ± 0.09	2.51 ± 0.07	− 2.01 ± 0.09
1028	133.800	34.738	0.50 ± 0.06	0.34 ± 0.07	1.49 ± 0.06	0.47 ± 0.07
1029	133.973	34.590	− 0.91 ± 0.07	0.41 ± 0.07	0.30 ± 0.07	0.56 ± 0.07
1032	133.341	34.612	− 0.37 ± 0.11	1.61 ± 0.10	0.92 ± 0.11	1.79 ± 0.10
1135	133.700	35.490	6.24 ± 0.06	− 0.87 ± 0.07	5.77 ± 0.06	− 0.75 ± 0.07
1167	134.492	35.536	4.21 ± 0.07	− 1.05 ± 0.10	3.14 ± 0.07	− 1.09 ± 0.10
1180	134.330	35.587	5.45 ± 0.07	− 0.95 ± 0.08	4.34 ± 0.07	− 0.95 ± 0.08
1187	133.339	35.435	5.58 ± 0.06	− 0.67 ± 0.06	5.44 ± 0.06	− 0.50 ± 0.06
HNKS	133.386	35.208	2.04 ± 0.15	− 1.43 ± 0.13	2.29 ± 0.21	− 1.29 ± 0.19
ISIM	134.804	33.843	− 19.60 ± 0.34	8.23 ± 0.30	− 17.07 ± 0.49	8.72 ± 0.43
KRKG	133.755	35.371	4.19 ± 0.11	− 1.20 ± 0.15	3.96 ± 0.15	− 1.10 ± 0.22
KRKH	133.845	35.450	5.87 ± 0.10	− 1.83 ± 0.10	5.41 ± 0.15	− 1.74 ± 0.14
KRNS	133.803	35.426	4.97 ± 0.11	− 1.34 ± 0.11	4.58 ± 0.16	− 1.25 ± 0.16
MNKK	133.721	35.081	1.21 ± 0.10	− 0.66 ± 0.11	1.58 ± 0.15	− 0.56 ± 0.16
MNYB	133.731	35.174	1.81 ± 0.13	− 0.70 ± 0.15	1.99 ± 0.18	− 0.60 ± 0.21
NNHS	133.323	35.337	4.03 ± 0.11	0.01 ± 0.12	4.08 ± 0.16	0.17 ± 0.17
NNIW	133.358	35.112	1.17 ± 0.16	− 1.09 ± 0.14	1.60 ± 0.23	− 0.94 ± 0.20
P118	134.316	35.594	5.63 ± 0.07	− 0.74 ± 0.08	4.53 ± 0.07	− 0.73 ± 0.08
SMSK	133.231	35.543	5.72 ± 0.14	− 0.55 ± 0.11	5.43 ± 0.20	− 0.34 ± 0.16

Table 1 (continued)

Station name	Longitude (°)	Latitude (°)	Uncorrected velocities		Corrected velocities	
			E–W (mm/year)	N–S (mm/year)	E–W (mm/year)	N–S (mm/year)
TTKH	134.200	35.401	2.00 ± 0.15	− 1.53 ± 0.13	1.46 ± 0.21	− 1.50 ± 0.18
TTKZ	134.202	35.447	3.53 ± 0.13	− 0.98 ± 0.12	2.87 ± 0.19	− 0.96 ± 0.17
TTSK	134.198	35.503	3.63 ± 0.16	− 1.22 ± 0.11	2.83 ± 0.22	− 1.20 ± 0.15
TTTG	134.185	35.470	3.70 ± 0.17	− 0.45 ± 0.16	2.99 ± 0.23	− 0.42 ± 0.22

Takada 2017). Anomalous stations, where the velocities are inconsistent with the observations at neighboring stations, are also identified as outliers within the area (gray arrows, Fig. 1). Data from these stations are not used in our analysis.

Velocity profiles across the SSZ for the component parallel to the zone indicate clear velocity gradients within a width of 50 km (Fig. 2). Velocity gradients around the area have been explained by Nishimura and Takada (2017) using an elastic dislocation. However, this model did not provide information about the width of the inelastic deformation in the lower crust. In order to tackle this issue, we proceed as follows.

Previous studies about deformation at strike–slip faults have assumed the existence of weak ductile shear zones beneath them (e.g., Prescott and Nur (1981); Yamasaki et al. (2014)). Similarly, the observed deformation around the SSZ can be explained by an elastic response to an inelastic deformation in the lower crust beneath the SSZ. We assume that this inelastic deformation can be approximated by dislocations of multiple parallel discrete faults distributed below the seismogenic depth. The faults are represented by n vertical dislocation planes, parallel to the SSZ, embedded in a homogeneous elastic half space with pure right-lateral motion. The dislocations are allowed to creep from a locking depth to infinite. We consider that the horizontal width of the inelastic deformation below the SSZ is represented by the distance between the first and the nth dislocation used for the model. We assume no variations along the strike of the fault, and solve the two-dimensional problem. In this, the locking depth, location of the deformation (horizontal location and width), and relative motion between the two blocks sandwiching the zone are the unknowns.

We apply a grid search algorithm to estimate the locking depth and horizontal location of the inelastic deformation, and then optimized the far-field relative velocities to fit the observations by minimizing the sum of squared residuals. Lastly, the Chi-squared residuals (χ^2) between the observation and the optimum models are used to assess the fit of the model.

There is a trade-off among the estimated locking depth, the width, and relative motion across the inelastic zone
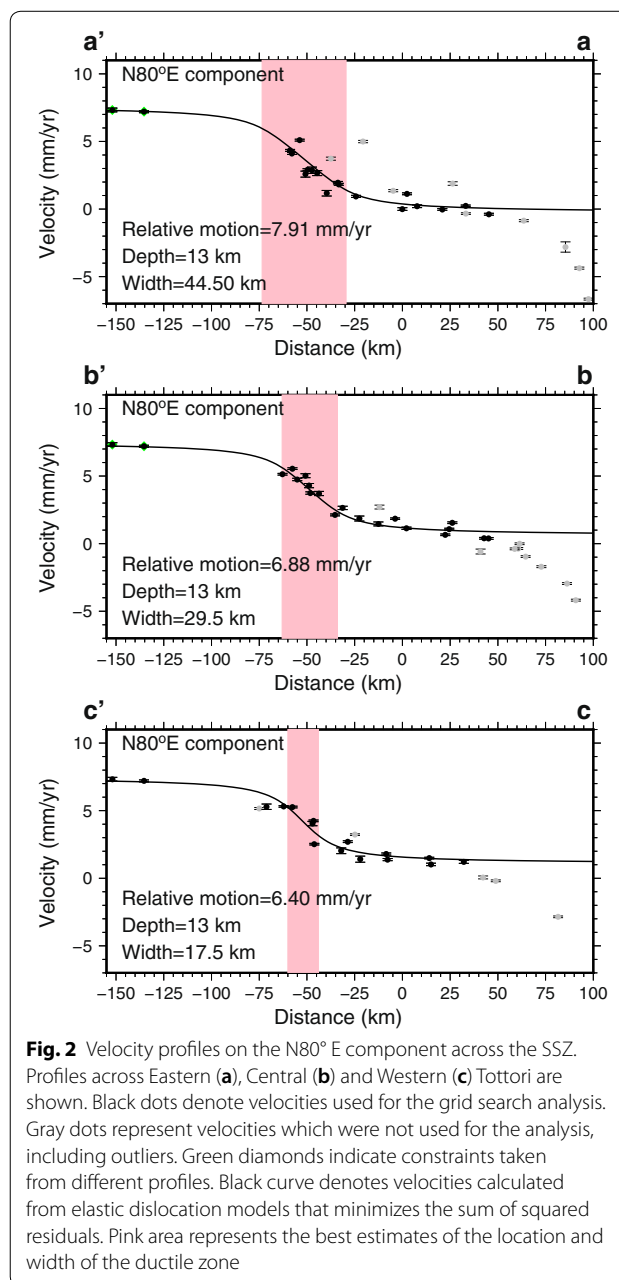

Fig. 2 Velocity profiles on the N80° E component across the SSZ. Profiles across Eastern (**a**), Central (**b**) and Western (**c**) Tottori are shown. Black dots denote velocities used for the grid search analysis. Gray dots represent velocities which were not used for the analysis, including outliers. Green diamonds indicate constraints taken from different profiles. Black curve denotes velocities calculated from elastic dislocation models that minimizes the sum of squared residuals. Pink area represents the best estimates of the location and width of the ductile zone

in the lower crust due to the limited resolution of the GNSS data (Additional file 2: Figure S2, Additional file 3: Figure S3 and Additional file 4: Figure S4). It is almost impossible to estimate both the locking depth and width precisely from the surface deformation because they are highly correlated (Additional file 2: Figure S2, Additional file 3: Figure S3 and Additional file 4: Figure S4). Deepening the locking depth is almost equivalent to widening the inelastic zone. Thus, we assume the locking depth to be 13 km, based on the cutoff depth of crustal seismicity (Omuralieva et al. 2012).

In our model, the dislocation planes are separated horizontally by 0.5 km, and distributed within 0–150 km width, which means we use between 1 and 301 dislocations to fit the model. Horizontal location of the western end of the deformation zone is varied every 0.5 km from −200 to 20 km (scale in Fig. 2). We constrain the optimum relative motion to be less than 10 mm/year taking into account the small relative velocity between Southwest Japan and the Korean Peninsula (e.g., Nishimura et al. 2018).

We focus on deformation along three profiles, which correspond to Eastern, Central and Western Tottori (Fig. 2). Because there are limited data to the north in Eastern and Central Tottori, we incorporate data from stations 0382 (36.29° N, 133.24° E) and 0383 (36.09° N, 132.98° E) on offshore islands in the models for those two profiles, as a maximum constraint of the displacement rate distribution (Figs. 1 and 2).

Once the minimum χ^2 has been found, we proceed to estimate the confidence interval of the parameters using the bootstrapping method with replacement. From each observation set, we create 1000 resample sets and estimate the optimum parameters for each configuration under the same constraints as for the original data sets. Then, we estimate an empirical cumulative probability function for each parameter based on their frequency distribution, and finally estimate the confidence interval based on the bootstrap percentile intervals. We present confidence intervals at a 68% level.
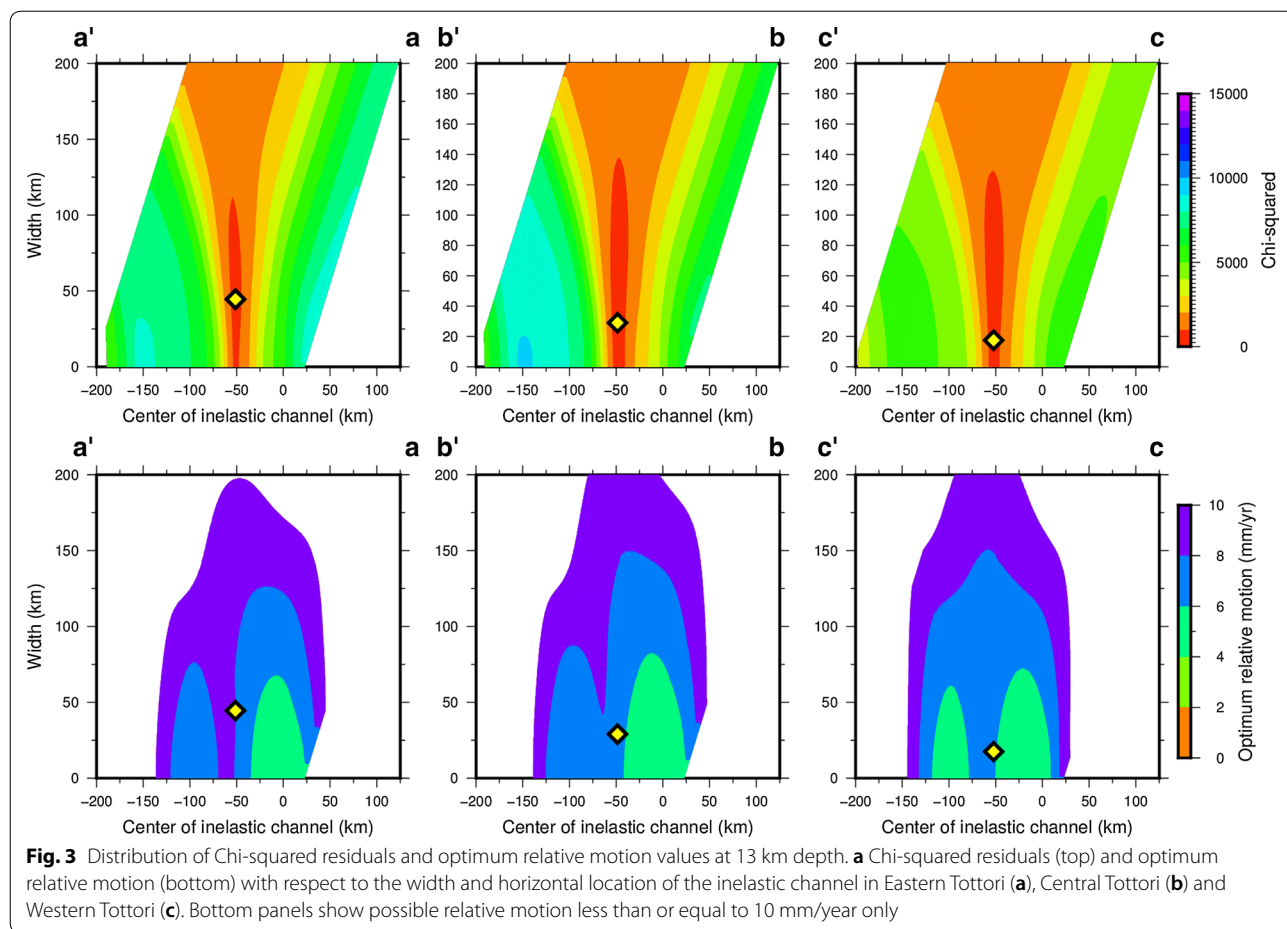
Results and discussion

We estimate the width of the inelastic deformation in the lower crust in the SSZ by assuming parallel vertical dislocation planes below 13 km depth (Omuralieva et al. 2012). Optimum models based on the horizontal displacement for the analyzed time period along three profiles suggest the relative speeds of 6.4–7.9 mm/year for the blocks sandwiching the deformation zones in Eastern, Central and Western Tottori (Fig. 2). The center of the inelastic deformation is seemingly constant along all the

profiles, while the width changes significantly from East to West (44.5–17.5 km) (Fig. 2). The Chi-squared residuals are not distributed along a quadric surface, which means that this is not a linear problem (Fig. 3). Thus, we evaluate the confidence level of the estimations using the bootstrap method. The 68% confidence level estimated from the bootstrap test indicates far-field relative motion between the blocks of 6.2–8.0 mm/year, and widths of 0.5–56.0 km, 0.5–79.5 km, and 0.0–58.5 km, for Eastern, Central and Western Tottori, respectively (Fig. 4), indicating that the geodetic measurement provides limited constraints on the inelastic deformation beneath the SSZ.

Several large earthquakes have occurred within the SSZ in the last century. Although our estimated inelastic deformation zone in the lower crust has large uncertainties of the width, the estimated zones are comparable with the source regions of large earthquakes in each profile, that is, the 1943 Tottori (M_j 7.2), the 2000 Western Tottori (M_j 7.3) and the 2016 Central Tottori (M_j 6.6) earthquakes (Fig. 1). A source fault and surface rupture of the 1943 earthquake (Kanamori 1972) is parallel to the SSZ and almost coincides with the center of our estimated inelastic deformation for Eastern Tottori. The source faults of the 2016 and 2000 earthquakes (Meneses-Gutierrez et al. 2019; Sagiya et al. 2002) in western and central profiles are conjugate with the SSZ and no surface ruptures appeared for the earthquakes. The 2016 earthquake occurred in the estimated inelastic zone, while the 2000 western Tottori earthquake extended to the south of the estimated zone, although an earthquake within the seismogenic depths might occur in a wider zone than the shear zone beneath it. Kawanishi et al. (2009) analyzed the spatial changes of the stress field in the SSZ based on the distribution of focal mechanisms in the area and found that the azimuth of the maximum compressional principal stress axes to the north of the mainshock of the 2000 Western Tottori earthquake are oriented in the WNW–ESE, while those in the south are oriented in the EW direction. They stated that the change of orientation of the principal stress could be related with the existence of a ductile fault zone beneath it. Our estimated inelastic deformation zone is in agreement with the location of their fault zone.

Low seismic velocity and low electrical resistivity zones in the lower crust are often related with ductile shear (e.g., Nakajima and Hasegawa 2007). A study of seismic tomography (Matsubara et al. 2008) shows low-velocity zones of P and S wave at a depth of 20 km around the SSZ. Recently Tsuda et al. (2019) have identified a low-velocity zone of P wave at a depth of 25 km beneath the SSZ and suggests the low-velocity zone in
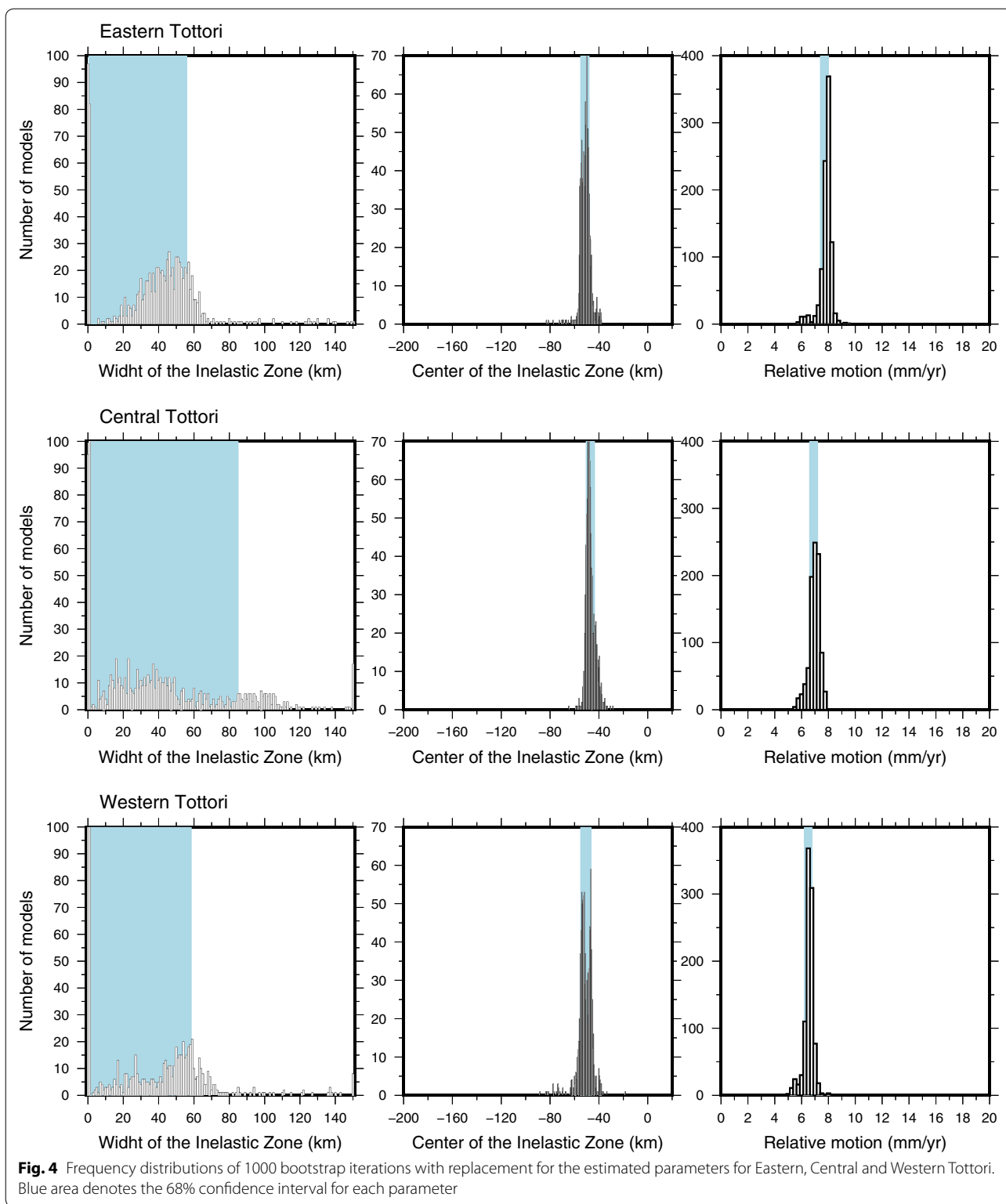
Fig. 3 Distribution of Chi-squared residuals and optimum relative motion values at 13 km depth. **a** Chi-squared residuals (top) and optimum relative motion (bottom) with respect to the width and horizontal location of the inelastic channel in Eastern Tottori (**a**), Central Tottori (**b**) and Western Tottori (**c**). Bottom panels show possible relative motion less than or equal to 10 mm/year only

the lower crust is attributed to high temperature due to a hot mantle upwelling below the low-velocity zone. These low-velocity zones are apparently ∼ 30–50 km wide, but it is difficult to discuss the real width of the low-velocity zone because of their limited spatial resolution (0.2°–0.3°). Low-resistivity zones in the lower crust have been also found beneath the SSZ (Shiozaki et al. 2006). However, it is also difficult to compare them with our inelastic deformation because the resistivity resolved by magnetotelluric data is mainly limited to a depth of ≤ 20 km.

A variation of the locking depth also controls how deformation concentrates around the shear zone (Additional file 2: Figure S2, Additional file 3: Figure S3 and Additional file 4: Figure S4). A wider channel for Central Tottori may be alternatively interpreted by the deepest locking depth. Efforts on combining

geophysical and geological data including GNSS, seismic wave structure, resistivity structure, focal mechanisms of earthquakes, and fault mapping can improve our understanding of deformation in the shear zone.

Conclusions

We analyze GNSS data within the SSZ to elucidate the crustal deformation mechanism of the shear zone in the lower crust under the assumption of inelastic deformation. Kinematic models based on the horizontal velocities from 2014 to December 2018 indicate that deformation in the area can be explained by an inelastic zone in the lower crust with a relative motion of 6.2–8.0 mm/year. Although uncertainties of the parameters are large, the width of inelastic zone in the lower crust at a 68% confidence level is narrower than 80 km, with the inelastic zone becoming thinner to the west.

Fig. 4 Frequency distributions of 1000 bootstrap iterations with replacement for the estimated parameters for Eastern, Central and Western Tottori. Blue area denotes the 68% confidence interval for each parameter

Changes in the locking depth of the kinematic models might provide alternative interpretations to the width of the inelastic deformation. Location of the inelastic channel is in agreement with the source regions of the recent large earthquakes in the area. Available GNSS data provide limited constraints on the deformation pattern.

Supplementary information

Supplementary information accompanies this paper at https://doi.org/10.1186/s40623-020-1138-z.

Additional file 1: Figure S1. a) GNSS velocities in and around the San-in Shear Zone from January 2014 to December 2018 before correcting for the postseismic deformation of the 2011 Tohoku-oki earthquake. Red diamond represents the reference site used for velocity calculation. Thin black lines denote active Quaternary fault traces (Research Group for Active Faults of Japan 1991). The inset figure shows the location of the study area with respect to the Japanese Islands. b) Velocity profiles across the SSZ on rectangle in figure a). Trend across the region, with higher gradient to the north of the profile is shown. This pattern reflects the postseismic relaxation of the 2011 Tohoku-oki earthquake, and its effect is corrected employing the viscoelastic model 4 in Suito (2017).

Additional file 2: Figure S2. Distributions of chi-squared residuals in Eastern Tottori when locking depth is a free parameter in the model calculation. Red diamond indicates the model that minimized the sum of the squared residuals.

Additional file 3: Figure S3. Distributions of chi-squared residuals in Central Tottori when locking depth is a free parameter in the model calculation. Red diamond indicates the model that minimized the sum of the squared residuals.

Additional file 4: Figure S4. Distributions of chi-squared residuals in Western Tottori when locking depth is a free parameter in the model calculation. Red diamond indicates the model that minimized the sum of the squared residuals.

Abbreviations
DPRI: Disaster Prevention Research Institute; GEONET: GNSS Observation Network System; GYPSY-OASIS: GNSS-Inferred Positioning System and Orbit Simulation Software; GNSS: Global Navigation Satellite System; GSI: Geospatial Information Authority of Japan; M_w: moment magnitude; SSZ: San-in Shear Zone.

Authors' contributions
Both authors participated in the design of the study. AMG conducted the analysis and wrote the manuscript. TN helped interpreting the data and revised the manuscript. Both authors read and approved the final manuscript.

Availability of data and materials
GNSS RINEX files for GEONET sites are available from the GSI website with registration (http://terras.gsi.go.jp/). Data from DPRI sites are available from the second author (TN). Velocity data from GNSS sites for the analyzed period are presented in a table within the manuscript.

Ethics approval and consent to participate
Not applicable.

Consent for publication
Not applicable.

Competing interests
The authors declare that they have no competing interests.

Author details
[1] Institute for Advanced Research, Nagoya University, Nagoya, Japan. [2] Disaster Mitigation Research Center, Nagoya University, Nagoya, Japan. [3] Disaster Prevention Research Institute, Kyoto University, Uji, Japan.

References
Akaike H (1974) A new look at the statistical model identification. IEEE Trans Autom Control 19(6):716–723. https://doi.org/10.1109/TAC.1974.1100705

Bertiger W, Desai S, Haines B, Harvey N, Moore AW, Owen S, Weiss JP (2010) Single receiver phase ambiguity resolution with GPS data. J Geodesy 84:327–337. https://doi.org/10.1007/s00190-010-0371-9

Bürgmann R, Dresen G (2008) Rheology of the lower crust and upper mantle: evidence from rock mechanics, Geodesy, and field observations. Annu Rev Earth Planet Sci 36:531–567. https://doi.org/10.1146/annurev.earth.36.031207.124326

Kanamori H (1972) Determination of effective tectonic stress associated with earthquake faulting. The Tottori earthquake of 1943. Phys Earth Planet Inter 5:426–434

Kawanishi R, Iio Y, Yukutake Y, Shibutani T, Katao H (2009) Local stress concentration in the seismic belt along the Japan Sea coast inferred from precise focal mechanisms: implications for the stress accumulation process on intraplate earthquake faults. J Geophys Res Solid Earth. https://doi.org/10.1029/2008JB005765

Marone CJ, Scholtz CH, Bilham R (1991) On the mechanics of earthquake afterslip. J Geophys Res 96(B5):8441

Matsubara M, Obara K, Kasahara K (2008) Three-dimensional P- and S-wave velocity structures beneath the Japan Islands obtained by high-density seismic stations by seismic tomography. Tectonophysics 454(1–4):86–103

Meneses-Gutierrez A, Nishimura T, Manabu H (2019) Coseismic and post-seismic deformation of the 2016 Central Tottori earthquake and its slip model. J Geophys Res Solid Earth 124(2):2202–2217. https://doi.org/10.1029/2018JB016105

Nakajima J, Hasegawa A (2007) Deep crustal structure along the Niigata-Kobe Tectonic Zone, Japan: its origin and segmentation. Earth Planets Space 59(2):e5–e8. https://doi.org/10.1186/bf03352677

National Research Institute for Earth Science and Disaster Resilience (2011) Broadband seismograph network (F-net). http://www.fnet.bosai.go.jp/event/tdmt.php?_id=20110311054500&LANG=en

National Research Institute for Earth Science and Disaster Resilience (2016a) Broadband seismograph network (F-net). http://www.fnet.bosai.go.jp/event/tdmt.php?_id=20160415162400&LANG=en

National Research Institute for Earth Science and Disaster Resilience (2016b) Broadband seismograph network (F-net). http://www.fnet.bosai.go.jp/event/tdmt.php?_id=20161021050600&LANG=en

Nishimura T, Takada Y (2017) San-in shear zone in southwest Japan, revealed by GNSS observations. Earth Planets Space 69:85. https://doi.org/10.1186/s40623-017-0673-8

Nishimura T, Yokota Y, Tadokoro K, Ochi T (2018) Strain partitioning and inter-plate coupling along the northern margin of the Philippine Sea plate, estimated from Global Navigation Satellite System and Global Positioning System-Acoustic data. Geosphere 14(2):535–551. https://doi.org/10.1130/GES01529.1

Omuralieva AM, Hasegawa A, Matsuzawa T, Nakajima J, Okada T (2012) Lateral variation of the cutoff depth of shallow earthquakes beneath the Japan Islands and its implications for seismogenesis. Tectonophysics 518–521:93–105. https://doi.org/10.1016/j.tecto.2011.11.013

Prescott WH, Nur A (1981) The accommodation of relative motion at depth on the San Andreas Fault System in California. J Geophys Res 86:999–1004. https://doi.org/10.1029/JB086iB02p00999

Research Group for Active Faults of Japan (1991) Active faults in Japan: sheet maps and inventories, revised edn. University of Tokyo Press, Tokyo (in Japanese with English summary)

Sagiya T, Miyazaki S, Tada T (2000) Continuous GPS array and present-day crustal deformation of Japan. Pure Appl Geophys 157:2303–2322. https://doi.org/10.1007/PL00022507

Sagiya T, Nishimura T, Hatanaka Y, Fukuyama E, Ellsworth W (2002) Crustal movements associated with the 2000 Western Tottori Earthquake and its fault models. Jishin 2:523–534 **(in Japanese)**

Savage JC, Burford RO (1973) Geodetic determination of relative plate motion in central California. J Geophys Res 78(5):832–845

Shiozaki I, Oshiman N, Uyeshima M, Murakami H, Yamaguchi S, Sakanaka S, Yoshimura R, Kuwaba Y, Yokoyama T (2006) A two dimensional resistivity structure beneath the seismic gap in the eastern part of Shimane prefecture, San-in region, Japan. In: Paper presented at 18th International Workshop on Electromagnetic Induction in the Earth, NSF, El Vendrell, Spain, 17–23 September

Suito H (2017) Importance of rheological heterogeneity for interpreting viscoelastic relaxation caused by the 2011 Tohoku-Oki earthquake. Earth Planets Space 69:21. https://doi.org/10.1186/s40623-017-0611-9

Tsuda H, Iio Y, Shibutani T (2019) Origin of the seismic belt in the San-in district, southwest Japan, inferred from the seismic velocity structure of the lower crust. Earth Planets Space 71:109. https://doi.org/10.1186/s40623-019-1091-x

Wessel P, Smith WHF (1998) New, improved version of the generic mapping tools released. EOS Trans Am Geophys Union 79:47. https://doi.org/10.1029/98EO00426

Yamasaki T, Wright TJ, Houseman GA (2014) Weak Ductile shear zone beneath a major strike-slip fault: inferences from earthquake cycle model constrained by geodetic observations of the western North Anatolian Fault Zone. J Geophys Res Solid Earth 119:3678–3699. https://doi.org/10.1002/2013JB010347

Yoshioka S, Matsuoka Y (2013) Interplate coupling along the Nankai Trough, southwest Japan, inferred from inversion analyses of GPS data: effects of subducting plate geometry and spacing of hypothetical ocean-bottom GPS stations. Tectonophysics 600:165–174. https://doi.org/10.1016/j.tecto.2013.01.023

Zhang X, Sagiya T (2017) Shear strain concentration mechanism in the lower crust below an intraplate strike-slip fault based on rheological laws of rocks. Earth Planets Space 69:82. https://doi.org/10.1186/s40623-017-0668-5

Zumberge JF, Heflin MB, Jefferson DC, Watkins MM (1997) Precise point positioning for the efficient and robust analysis of GPS data from large networks. J Geophys Res 102(B3):5005–5017. https://doi.org/10.1029/96jb03860

Publisher's Note